Acta Materialia 245 (2023) 118612

Contents lists available at ScienceDirect

Acta Materialia

journal homepage: www.elsevier.com/locate/actamat

Martensitic transformation during electrochemical polishing of metastable austenitic stainless steel

Hojun Gwon [a,1], Junyoung Chae [b,1], Chanwoo Jeong [b], Hyukjae Lee [b], Dong Hwi Kim [a], Sam Yaw Anaman [c], Dameul Jeong [d], Hoon-Hwe Cho [c], Young-Kyun Kwon [d], Sung-Joon Kim [a,*], Heung Nam Han [b,*]

[a] Graduate Institute of Ferrous Technology, Pohang University of Science and Technology, Pohang 37673, Republic of Korea
[b] Department of Materials Science and Engineering & Research Institute of Advanced Materials, Seoul National University, Seoul 08826, Republic of Korea
[c] Department of Materials Science and Engineering, Hanbat National University, Daejeon 34158, Republic of Korea
[d] Department of Physics and Research Institute for Basic Sciences, Kyung Hee University, Seoul 02447, Republic of Korea

ARTICLE INFO

Keywords:
Martensitic transformation
Electrochemical polishing
Electroplasticity
Multiphysics simulation
First-principles calculations

ABSTRACT

We found that remarkable martensitic transformation occurs during electrochemical polishing (EP) in 16Cr-5Ni metastable austenitic stainless steel. It was observed through EBSD measurement that the α' martensite fraction increases as the applied voltage and EP time increase. Interestingly, upon comparing EBSD, XRD, and ferritescope measurements, it was confirmed that the martensitic transformation is confined to the surface where EP took place. To investigate the mechanism by which the EP process induces the martensitic transformation, COMSOL Multiphysics was used to calculate the electric charge distribution on the specimen surface under various applied voltages. In order to accurately consider the surface shape of the specimen, we used AFM for measurement of the three-dimensional space distribution of asperities, which was utilized as an initial condition of COMSOL Multiphysics simulation. Finally, through the first-principles calculations reflecting the obtained charge distribution in the surface region, it was concluded that significant stress could be developed due to the charge build-up on the surface, resulting in stress-induced martensitic transformation on the surface of the metastable austenitic stainless steel during EP.

1. Introduction

Electrochemical polishing (EP) creates a mirror-like surface by selectively removing specific parts such as asperities and oxides from the surface region of a workpiece. When an electric voltage is applied to an acidic solution, the ions on the metal surface dissolve, leaving behind a mirror-like surface. Because EP does not apply an external force and/or a deformation that may seriously alter the surface characteristics of metallic specimens in comparison to mechanical polishing [1] or focused ion beam milling [2–4], it has been widely utilized as a process of preparing a metal specimen for accurate microstructure observation. Although EP is only a process that causes an electrochemical reaction by applying an electric current to the specimen surface at anode; interestingly, however, it has been observed that a remarkable α' martensitic transformation occurs during EP treatment in several metastable austenitic stainless steels, although the occurrence of martensitic transformation at cathode during electrochemical hydrogen charging had been reported [5]. In this study, therefore, the characteristics of α' martensitic transformation occurring during EP were analyzed and its mechanism was proposed.

Recently, numerous research studies have been carried out on applying electric current and/or electric charge to significantly change the microstructure or mechanical properties of metallic materials [6–8]. Especially, electroplastic phenomenon has demonstrated that the elongation increases remarkably during deformation under electric current without significant temperature rise due to Joule heating [9–11]. In addition, several studies have been conducted to explain the mechanism of electroplasticity. Lahiri et al. [12] presented the mechanism of electroplasticity by comparing thermal softening, electron-wind force, and paramagnetic depinning of dislocations based on a crystal plasticity

* Corresponding authors.
E-mail addresses: sjkim1@postech.ac.kr (S.-J. Kim), hnhan@snu.ac.kr (H.N. Han).
[1] These authors contributed equally to this work.

https://doi.org/10.1016/j.actamat.2022.118612
Received 27 July 2022; Received in revised form 8 December 2022; Accepted 10 December 2022
Available online 11 December 2022

model. They concluded that the reduced flow stress in electroplastic behavior is mainly induced by the depinning of dislocations from paramagnetic obstacles and Joule heating. Kim et al. [13] demonstrated the origin of electroplasticity based on first-principles calculation, microstructure-based finite element simulation, and experimental approaches. They suggested that the athermal effect of electric current could be explained by the weakening of atomic bonding strength near defects such as grain boundary, dislocation, free surface, and so on, which is induced by charge imbalance near the defects under electric current. Rudolf et al. [14] reported that dislocations, defects, and atoms can be scattered by thermal phonons through application of electric current, and both thermal phonon and electron effects can be a viable mechanism for electroplasticity.

Regarding electroplasticity, several researchers have reported that electric current can enhance the diffusion kinetics via its thermal as well as athermal effects [9,11,12]. Many research works have examined the effect of electric current on the microstructural changes in various metallic materials [15–19]. It has been confirmed that concrete microstructural changes such as annealing [20–22], aging [23–25], dissolution [26,27], healing [28,29], and recrystallization [30], can get accelerated via the athermal effect of electric current. Ghiotti et al. [20] observed a reduction in the dislocation density in 1050 aluminum alloy with the aid of the electroplastic effect. McNeff and Paul [23] reported that the rapid aging effect in electrically-assisted pulling of Haynes 230 can be demonstrated by electron-ion collision. Zheng et al. [27] identified an improved dissolution rate through the electropulsing treatment process for 6061 aluminum alloy with enhanced mechanical properties. Tang et al. [29] showed that electropulsing has a positive effect on the healing of microcracks and microvoids in 2024 aluminum alloy.

As mentioned above, many studies have reported that electric current and/or charge can have a considerable effect on the binding force between atoms near defects, which causes various microstructural changes including electroplastic phenomenon. Since EP is also a process in which a charge build-up is developed on the specimen surface via an electrochemical reaction, an α' martensitic transformation in a metastable austenitic stainless steel during EP may also be interpreted as a type of electric current-induced phenomenon. In this study, therefore, using EBSD, XRD, and ferritescope, it was confirmed whether α' martensitic transformation in a metastable austenitic stainless steel occurs under various EP conditions with various voltages and holding times. Moreover, to investigate the mechanism by which the EP process induces the α' martensitic transformation, we calculated the charge distribution on the stainless steel surface under various applied voltages using COMSOL Multiphysics [31]. For the accurate shape of the specimen surface, three-dimensional distribution of asperities was measured using AFM, which was used as an initial condition for the COMSOL Multiphysics simulation. Subsequently, we performed first-principles density functional theory calculations under the obtained charge distribution to explain the mechanism of metastable austenite transformation into α' martensite during the EP process.

2. Materials and experimental procedure

A 16Cr-5Ni-0.15C-0.1N-0.9Si-0.3Mn (wt.%) stainless steel was prepared using vacuum induction melting. The ingot was hot-rolled to a thickness of 3 mm, annealed at 1100 °C for 5 min, and then cold rolled to a thickness of 2.4 mm at a 20% reduction ratio. The EP treatment was conducted in a mixture of 10% perchloric acid and 90% acetic acid, and a voltage range of 20 to 40 V at room temperature; in order to avoid the effect of hydrogen intrusion during cathodic charging, the specimen was used as an anode for the EP treatment. After EP treatment on the surface of the cold-rolled specimen in the normal direction (ND), the specimen was sealed in a quartz tube in vacuum state to prevent oxidation during heat treatment as shown in Fig. S1 (supplementary material). The specimen in the sealed quartz tube was annealed at 1150 °C for 1 h to make 100% austenite phase and then cooled down via water quenching. The ND surface of the annealed specimen was further EP-treated to observe the effect of treatment time and applied voltage on the α' martensitic transformation (Fig. S1).

Microstructural analysis was performed using EBSD. A field emission scanning electron microscope (Carl Zeiss AG, ZEISS ULTRA-55, Germany) was used to collect the EBSD patterns. The volume fraction of α' martensite before and after EP was measured using XRD, EBSD, and Ferritescope (Fischer Technology, FMP30, USA). XRD analysis was performed using a Bruker D8-Advance Davinci (Bruker Company, Germany) equipped with a copper target that yielded 0.154 nm wavelength with a scan step of 0.01° for 1 s and scan angle $30^\circ \leq 2\theta \leq 105^\circ$. The phase fraction of α' martensite was obtained via Rietveld refinement using TOPAS software package [32].

During EP treatment, chemical reactions occur on the surface of the specimen and are closely related to the shape of the surface [33]. Hence, the shape of the specimen surface was quantified three-dimensionally, as shown in Fig. 1, using atomic force microscopy (AFM, Park Systems, NX-10, South Korea) with a resolution of 0.05 nm [34]. To obtain parameters related to the morphological distribution of surface asperities, the scan area and speed were set to $3 \times 3\ \mu m^2$ and 0.3 Hz, respectively: the detailed measurement conditions are given in Table S1.

These surface roughness parameters were analyzed using XEI software package [35]. For the statistical evaluation of the shape and size of asperities, the root mean square deviation (R_q) and kurtosis (R_{ku}) of the surface roughness extracted through the line profile were used, as shown in the formulas below [36,37].

$$R_q = \sqrt{\frac{1}{l}\int_0^l Z^2(x)dx} \tag{1}$$

$$R_{ku} = \frac{1}{R_q^4}\left[\frac{1}{l}\int_0^l Z^4(x)dx\right] \tag{2}$$

Here, l and x denote the base length of asperity and the absolute horizontal coordinates within the base length, respectively, and $Z(x)$ represents the absolute vertical coordinates; the starting point of the line profile is taken as the origin of the coordinate axis.

3. Modeling for electrochemical polishing

3.1. Finite element (FE) model for electrochemical polishing

As shown in Fig. 2, when a specimen (anode) and a cathode electrode are immersed in the electrolyte during EP, a small amount of oxygen gas is generated at the anode, as the specimen dissolves. Concurrently, the dissolved metal ions in the electrolyte solution react with the asperities on the surface of the specimen to form an oxide layer and simultaneously cause the elution of more metal ions as the anodic dissolution progresses.

In the process of oxidation-reduction reaction on the surface, electrons flow into the surface of the specimen, from the anode to the cathode through an electric wire [38]. Acetic and perchloric acids were used as electrolytes to elute divalent metal cations during EP and form an oxide layer, metal perchlorate, and metal acetate. These hypothetical reactions are as shown below [39].

$$(CH_3COO)_2O + 3Me - 2e^- \rightarrow MeO + Me^{2+} + (CH_3COO)_2Me \tag{3}$$

$$2HClO_4 + Me - 2e^- \rightarrow Me(ClO_4)_2 + H_2 \tag{4}$$

From the above reaction, it can be affirmed that the number of perchlorate anions and acetate anions participating in the reaction during EP, on the one hand, and the number of electrons flowing into the metal specimen, on the other hand, are the same. Therefore, by calculating the areal ion charge density near the asperity, the areal electron

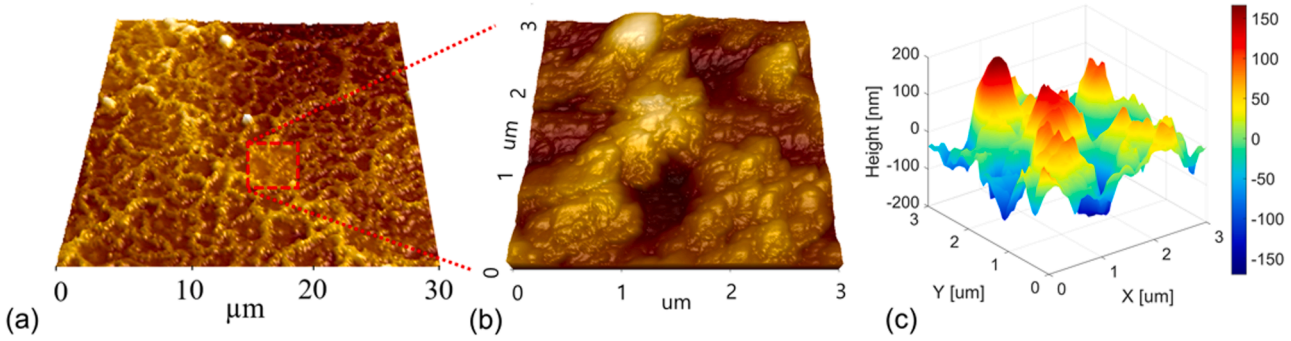

Fig. 1. Atomic force microscope (AFM) images for morphological analysis of asperity (a) The 3D image obtained for 30 × 30 μm^2 region, (b) 3D image obtained for 3 × 3 μm^2 region, and (c) Z-axis height distribution contour map for 3 × 3 μm^2 region.

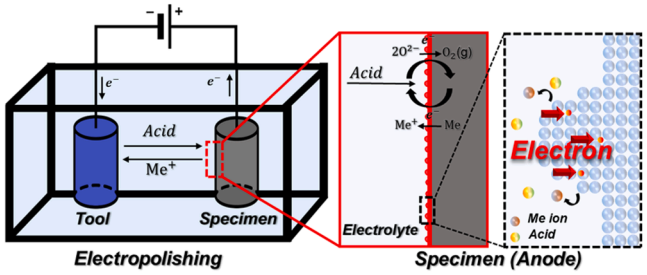

Fig. 2. Schematic diagram of electrochemical polishing (EP) and oxidation-reduction reactions occurring around the surface asperity of stainless steel specimen.

charge density flowing into the metal specimen can be obtained. A multiphysics-based simulation using COMSOL multiphysics was used to calculate the areal ion charge density.

In order to calculate the areal ion charge density concentrated on the surface asperity of stainless steel, a multiphysics-based simulation model as shown in Fig. 3 was established two-dimensionally assuming a columnar structure. The shape of asperity was set based on the surface roughness data of Eqs. (1) and (2), which were measured using AFM and analyzed statistically. As shown in Fig. 3a, the dimension of the specimen surface including asperity was set to 100 × 20 μm^2, and it was designed to be in contact with the electrolyte (90% acetic acid-10% perchloric acid) having the same dimension as the specimen. The base lengths (l) of asperity were set to 100, 300, 500, and 1000 nm based on the statistical analysis of AFM measurement data. The sharpness of asperity was set to 1.37, 1.58, 2.21, 3.34, and 4.75 based on the kurtosis (R_{ku}) of the surface roughness data (Fig. 3b). Based on the various morphological conditions of asperity, the effect of the asperity shape on areal ion charge density during EP treatment was calculated.

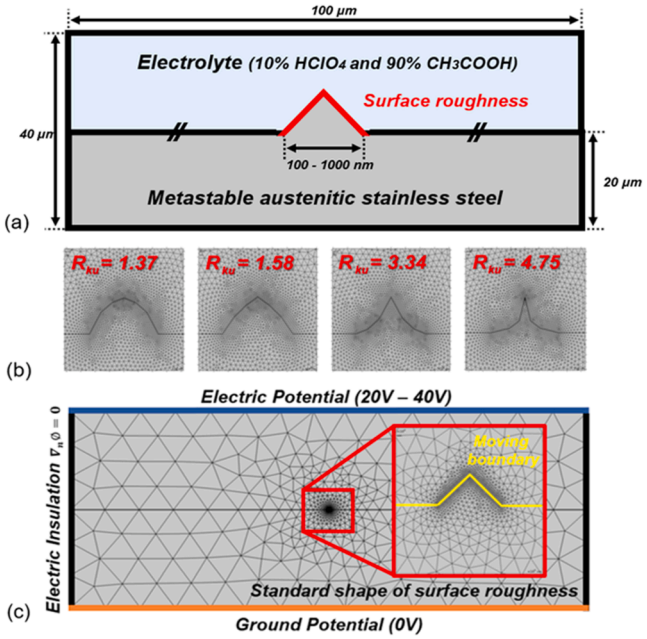

Fig. 3. Overview of the EP simulation model (a) Designed simulation conditions and dimensions for EP, (b) Differently defined asperities and their corresponding mesh conditions, and (c) Boundary conditions for EP simulation.

To ensure an accurate solution, more dense triangular elements were used as the upper vertex of the asperity approached. The same analysis was repeatedly performed while increasing the total number of meshes, and the mesh refinement proceeded until negligible changes were observed in the calculation result. The resulting mesh had a total of 15,832 triangular elements. For the electrical conductivity values used in the calculations, 37 S/m and 1.45 × 10^5 S/m were set for the electrolyte and stainless steel, respectively, and a relative permittivity of 18.5 was used for the electrolyte [40,41]. The relative permittivity of the acetic acid-perchloric acid mixed electrolyte at room temperature was obtained using the relative permittivity of fluid mixture law [42]. Meanwhile, the simulations were performed while fixing the lower boundary to the ground potential and changing the voltage applied on the upper boundary to 20, 30, and 40 V. In addition, the insulation condition was applied to the left and right boundary of the model so that the potential boundary did not exist (Fig. 3c).

The governing equation for the current conservation condition for calculating the areal ion charge density during EP treatment is as follows [43]:

$$J = \sigma E + \frac{\partial D}{\partial t} + J_e \tag{5}$$

where J, σ, E, D, t, and J_e represent current density, electrical conductivity, electric field, displacement field, time, and external current density, respectively. When the electrolyte is considered a linear isotropic material, the ions of the electrolyte are divided into bound charges and free charges by an external electric field [44]. The polarization properties of electrolytes can be defined through the following displacement fields [45]:

$$D = \varepsilon_0 \varepsilon_r E \tag{6}$$

where ε_0 and ε_r are the vacuum permittivity and the relative permittivity, respectively. The displacement field obtained through Eq. (6) was applied to the Gauss law of Eq. (7) and used to obtain the areal ion charge density [45].

$$\oint_s D \cdot da = \int_v \rho_f \cdot dt = q_{free} \tag{7}$$

where a, ρ_f, and q_{free} represent the cross-sectional area, free charge density, and flow charge amount, respectively.

To reflect the etching by external voltage during EP, the following boundary condition was used, which defines the interfacial mobility between the specimen and the electrolyte [46]:

$$U = -K \cdot J_n \tag{8}$$

where U, K, and J_n are the velocity of the interface, the coefficient of interface velocity, and the normal current density, respectively. The interfacial mobility of the specimen surface is proportional to the normal current density. In addition, the coefficient of interface velocity K is a material constant, and it was calibrated by using the R_q value statistically analyzed with AFM data. Its value was obtained as 3×10^{-19} m^3/As through a calibration.

3.2. Density functional theory calculations for excessive charge effect

To understand the experimentally observed martensitic transformation during electrochemical polishing of metastable austenitic stainless steel, we simplified it as a transformation from FCC to BCC structure of iron in the presence of excess charge. We constructed a supercell with six iron atoms of FCC in a cuboid, in which there are three (111) planes or ABC planes perpendicular to the c-axis or the [111] direction (Fig. 4a). Note that the a- and b-axes are parallel to the $[\bar{1}01]$ and $[\bar{1}2\bar{1}]$ directions, respectively (Fig. 4b). It is well known from the K-S relationship [47,48] that the (111) plane of the conventional FCC structure can be shared by the (110) plane of its BCC counterpart with an appropriate strain, as shown in Fig. 4b where the yellow and red boxes indicate the FCC (111) and BCC (110) planes, respectively.

To understand how excess charge induces stress on the structure resulting in the structural transformation, we performed first-principles calculations based on density functional theory, as implemented in the Vienna *ab initio* simulation package (VASP) [49–52]. Planewave basis was used to expand the electronic wave functions with a kinetic energy cutoff of 600 eV. Exchange-correlation functional was treated within the generalized gradient approximation of Perdew-Burke-Ernzerhof [53] with spin polarization. We employed the projector-augmented wave pseudopotentials [54] to describe the valance electrons. The Brillouin zone (BZ) corresponding to the supercell was sampled using a 29 × 51 × 21 k-point mesh according to the Monkhorst-Pack scheme [55]. We also used the first-order Methfessel-Paxton scheme [56] with a smearing width of 0.2 eV to integrate the BZ, since the scheme is known to well describe the partial occupancies near the Fermi level of metals. Excess charge calculations were performed with the same amount of uniformly-distributed opposite background charges to prevent divergence of the total energy due to infinitely-repeating excess charges in the periodic configuration. It turned out that all the parameters used in our calculations were optimally selected to evaluate accurate and converged values of total energy, force, stress tensor, and so on.

4. Results and discussion

4.1. Observation of martensitic transformation during electrochemical polishing

The 16Cr-5Ni-0.15C-0.1N-0.9Si-0.3Mn (wt.%) stainless steel specimen was annealed at 1150 °C for 1 h in a sealed quartz tube and then cooled down to room temperature via water cooling (Fig. S1). As shown in Fig. 5(a) obtained from EBSD, a specimen that had >40% α' martensite before annealing was changed to 100% austenite structure after annealing at 1150 °C for 1 h. The quartz sealing in a vacuum seems to effectively protect the EP-treated surface from oxidation during annealing. Further EP treatments were performed on the fully austenitic surface with the variation of the change of voltage level and duration, and the surface of the specimen was observed with EBSD (Fig. 5b). Interestingly, a significant amount of α' martensite was observed by EBSD analysis on the surface of the EP-treated specimen at anode: At a fixed voltage of 20 V, an increase in EP duration resulted in an increased α' martensite fraction. EP treatment for 40 s yielded 25.7% α' martensite on the surface, whereas EP treatment for 160 s yielded 72.2% α' martensite. EP treatment at 30 V yielded a higher fraction of α' martensite than that at 20 or 40 V. The smaller fraction of α' martensite after EP treatment at 40 V than at 30 V may be a result of the elimination of the phase transformed layer due to etching.

To examine the effect of specimen depth on the EP-induced α' martensitic transformation, the fraction of α' martensitic transformation was additionally measured using XRD and ferritescope on the same specimen. The XRD analysis results (Fig. 6a) revealed that the annealed specimen showed strong austenite (face-centered cubic structure) peaks, with relatively smaller α' martensite (body-centered cubic structure) peaks. As the EP treatment duration increased at a fixed voltage of 20 V, the intensity of the α (110) peak increased gradually (Fig. 6b). The fraction of α' martensite, which was calculated using the Reitveld method in TOPAS, gradually increased as the EP treatment duration increased, i.e., from 26.8% at 40 s to 45.6% at 160 s (Fig. 6c). The amount of α' martensitic transformation was also measured using a ferritescope. The total fraction of α' martensite converted from magnetic

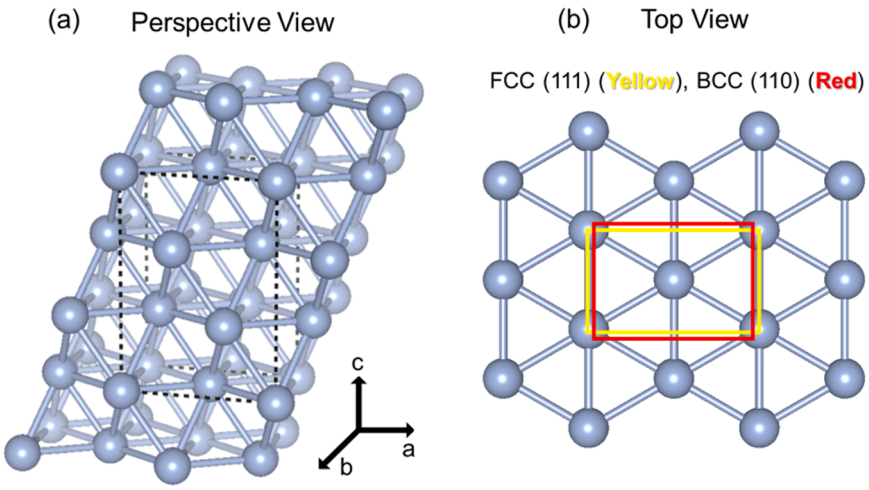

Fig. 4. Various views of iron structure for the DFT calculation (a) Supercell of FCC (111) bulk structure, (b) Top view of the supercell showing FCC (111) and BCC (110) planes, respectively.

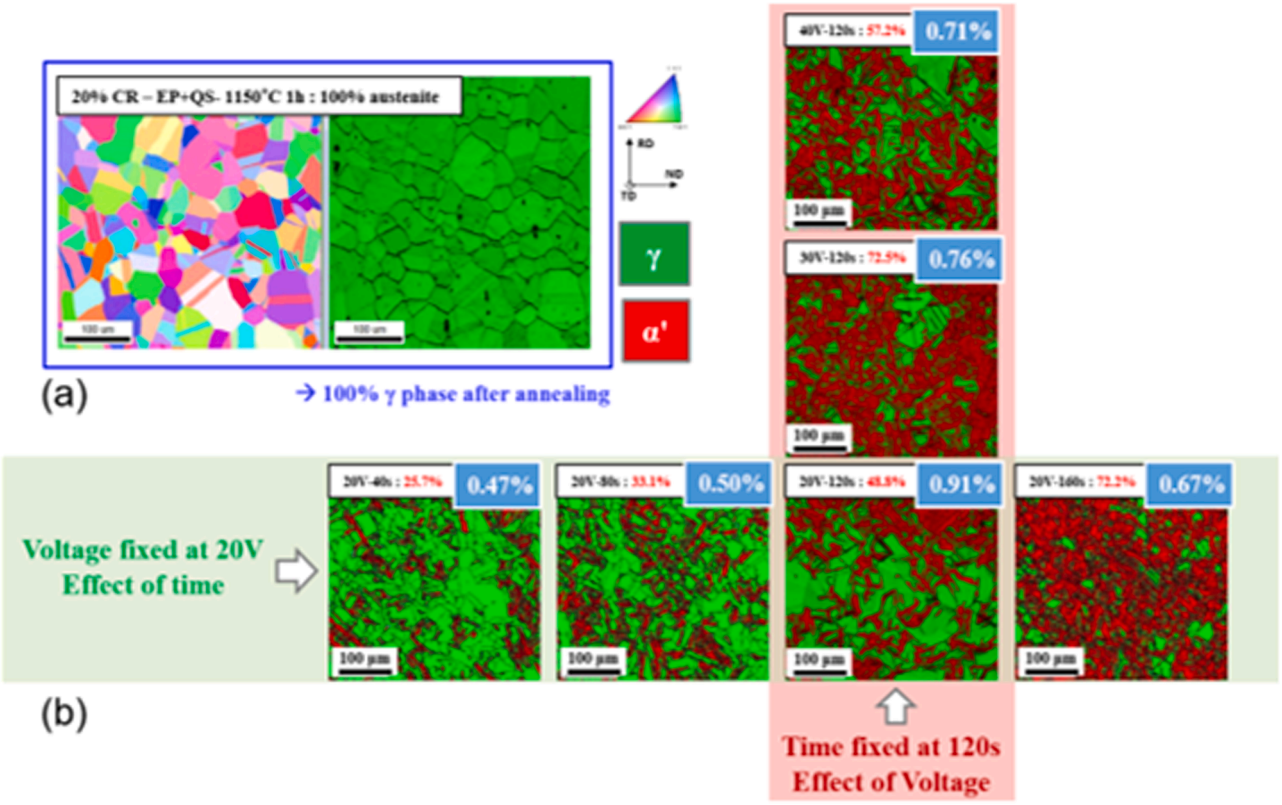

Fig. 5. Effect of EP treatment condition on martensitic transformation of 16Cr-5Ni-0.15C-0.1N-0.9Si-0.3Mn (wt.%) stainless steel (a) ND inverse pole figure map and phase map for specimen annealed at 1150 °C for 1 h, and (b) EBSD image with martensite fraction at various voltages (Vertical line: 20, 30, and 40 V) and EP duration (Horizontal line: 40, 80, 120, and 160 s).

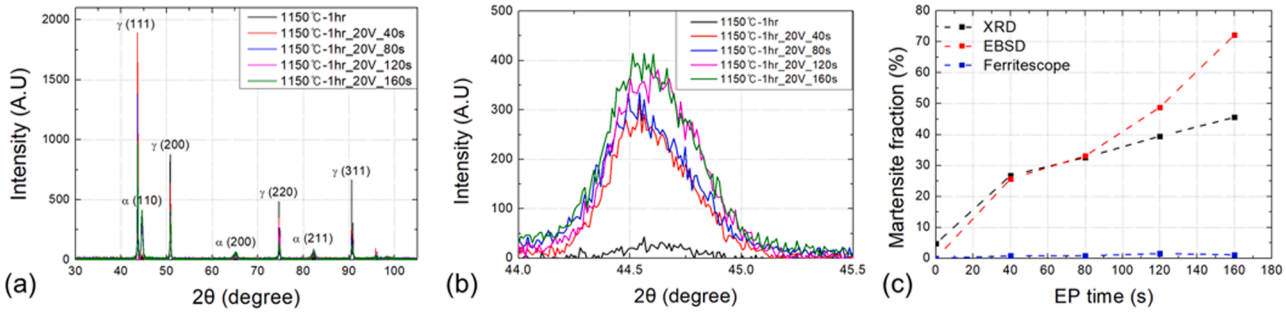

Fig. 6. XRD analysis results of EP-treated specimen after annealing at 1150 °C for 1 h. (a) whole XRD peaks of the annealed specimens with varying EP treatment time (Voltage of 20 V; 0, 40, 80, 120, and 160 s), (b) magnified α (110) peaks, and (c) α' martensite fraction calculated by XRD (Reitveld method), EBSD, and ferritescope.

saturation [57] from a penetration depth of 1-2 mm [58] was less than 1% in all EP duration conditions (Fig. 6c). Thus, the α' martensite fraction obtained from ferritescope measurement is much lower than those measured from EBSD and XRD. This result indicates that α' martensitic transformation was limited to the extreme surface of the specimen. Meanwhile, the difference between XRD and EBSD measurements might be attributed to the fact that XRD analysis has a larger interaction volume than EBSD [59].

Another experiment was performed on specimens with various compositions to verify that EP-induced α' martensitic transformation does not occur only in the specific composition of the steel. The specimens used in the experiment had similar chemical compositions, while the concentration of the main elements, i.e. Mn, Cr, and Ni, was slightly different. The experimental results and analysis for these specimens are presented in Table S2 and Fig. S2 of the supplementary material. As a result, it was identified that the martensitic transformation during EP is not limited to a specific composition of stainless steel.

4.2. Statistical analysis of surface roughness and FE simulation for EP

To investigate the mechanism of the α' martensitic transformation during EP, as described above, a multiphysics-based simulation using COMSOL multiphysics was used to calculate the charge distribution on the surface of stainless steel under various applied voltages. The three-dimensional space distribution of asperities was measured using AFM to accurately consider the shape of the specimen surface; subsequently, statistical analysis was performed based on the obtained surface roughness parameter data (Fig 7). Root mean square deviation (R_q), kurtosis (R_{ku}), and base length (l) of asperities are presented in Figs. 7a, 7b, and 7c, respectively, fitted with a lognormal distribution function

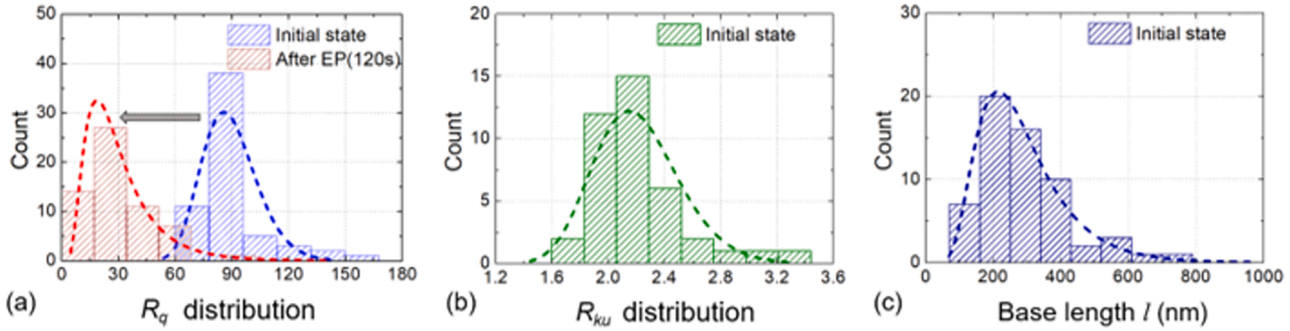

Fig. 7. Surface roughness parameters and base length of asperity statistically represented using lognormal distribution (a) Rq over time (0 and 120 s), (b) Rku, and (c) base length.

[60,61]. It can be seen that the R_q value gradually decreases with etching (Fig. 7a). Using the statistical results of Figs. 7b and 7c, the standard asperity was set as follows: kurtosis (R_{ku}) of 2.21 and base length (l) of 300 nm. In addition, using statistical data such as maximum, minimum, first quartile, and third quartile values of kurtosis (R_{ku}) and base length (l), representative asperities used in COMSOL Multiphysics simulation were designated in various shapes as described in Section 3.1.

The distribution of current density and areal ion charge density according to EP duration calculated is shown in Fig. 8 and Fig. S3. In Fig. 8a, the maximum current density of approximately 10^7 A/mm^2 is concentrated when a voltage of 40 V is applied for standard asperity. Both the sharpness of asperity and the maximum current density decreased as etching progressed. Fig. 8b shows the areal ion charge density (C/m^2) over EP duration. The amount of ion charge on the surface was largest at the tip of the asperity and diminished as the surface roughness decreased with etching.

By conducting simulations with various values of kurtosis (R_{ku}) and base length (l) for the asperities, the effect of asperity shape on the areal ion charge density was identified. These simulation results are shown in Tables S3 and S4, and summarized in Fig. 9. Under the base length (l) of 300 nm, as the R_{ku} value increased, the areal ion charge density increased linearly (Fig. 9a). Meanwhile, when the R_{ku} value was fixed at 2.21, it was confirmed that the areal ion charge density decreased exponentially as the base length increased (Fig. 9b).

As the R_{ku} value of asperity increases and the base length decreases, the tendency of the areal ion charge density to decrease was observed in all simulation conditions, regardless of the strength of the applied voltage. And it was also found that the factor that had a dominant influence on the areal ion charge density area was the base length, which means the size of the asperity, rather than the R_{ku} value of the asperity.

4.3. Excess charge effect on stress based on density functional theory simulation

To investigate the effects of excess charge on the structural transformation, we performed *ab initio* calculations based on density functional theory. We first estimated a realistic range of excess charge amounts in the Fe FCC structure by converting the areal ion charge density evaluated under various conditions of voltages and asperity shapes into the number of electrons per single Fe atom through the following procedure, which is also schematically described in Fig. 10. It was assumed that the calculated areal ion charge density is the same as the areal electron density flowing through asperity. Then, we calculated the number of electrons per Fe atom directly from the areal electron density under various voltage and shape conditions by considering the number density of Fe atoms in a (111) plane; they are summarized in Table 1. The number of electrons flowing in the standard asperity during EP was evaluated to be more than 10^{-3} per Fe atom. On the contrary, those flowing in asperities with a larger R_{ku} value or a smaller base length (l) can increase up to approximately 10^{-2} per Fe atom.

With these evaluated numbers of electrons per Fe atom in mind, we calculated the stress applied to the equilibrium unit cell while adding extra electrons to the FCC unit cell shown in Fig. 4a. We varied the amount of excess electrons from 10^{-5} to 10^{-1} per Fe atom. Note that the neutral Fe FCC unit cell was fully relaxed to have essentially zero stress. As shown in Fig. 11, we found that the applied stress depends logarithmically linearly on the excess electrons within a range of 10^{-5} and 10^{-1} electrons per Fe atom. More interestingly, the applied stress also depends algebraically linearly on the excess electrons with a slope of 1.55×10^{-5} MPa per electron.

It was shown that the evaluated numbers of 10^{-3} and 10^{-2} electrons per Fe atom flowing in asperities during EP can cause the applied stress estimated to be approximately 155 MPa and 1.55 GPa, respectively. This can be explained as the excess charge in a finite unit cell causes self-repulsive interaction resulting in structural stress and leads to possible structural transformation into the BCC structure. Therefore, in real situations, approximately 10^{-3} to 10^{-2} electrons per single Fe atom penetrated in metastable austenitic stainless steel during EP can trigger EP-induced stresses on the scales of hundreds to thousands of MPa.

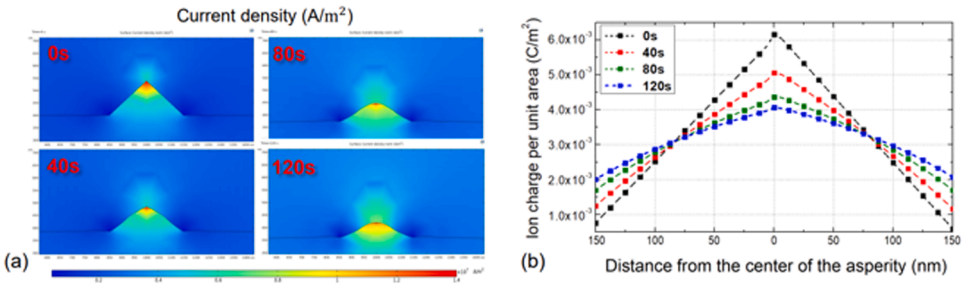

Fig. 8. Morphological change of surface asperity by etching over EP duration (0, 40, 80, and 120 s) (a) Contour map of current density distribution under application of 40 V, and (b) Areal ion charge density under application of 40 V.

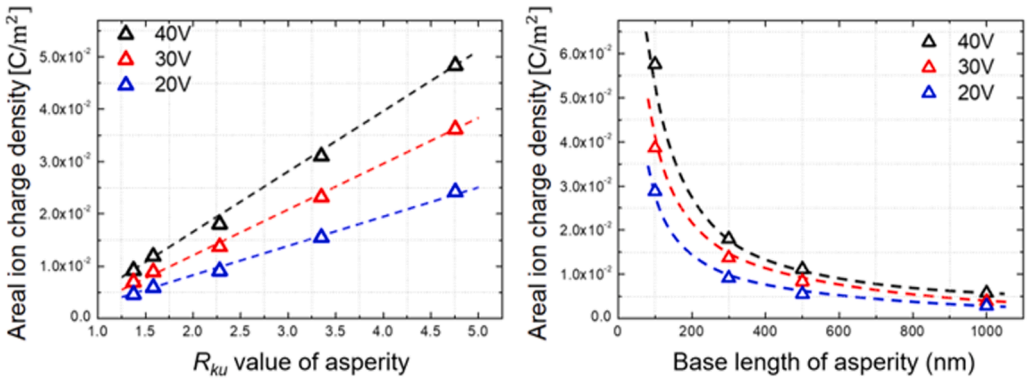

Fig. 9. Areal ion charge density according to the various shapes and sizes of asperity. (a) Areal ion charge density with various Rku values, and (b) Areal ion charge density with various base lengths of asperity.

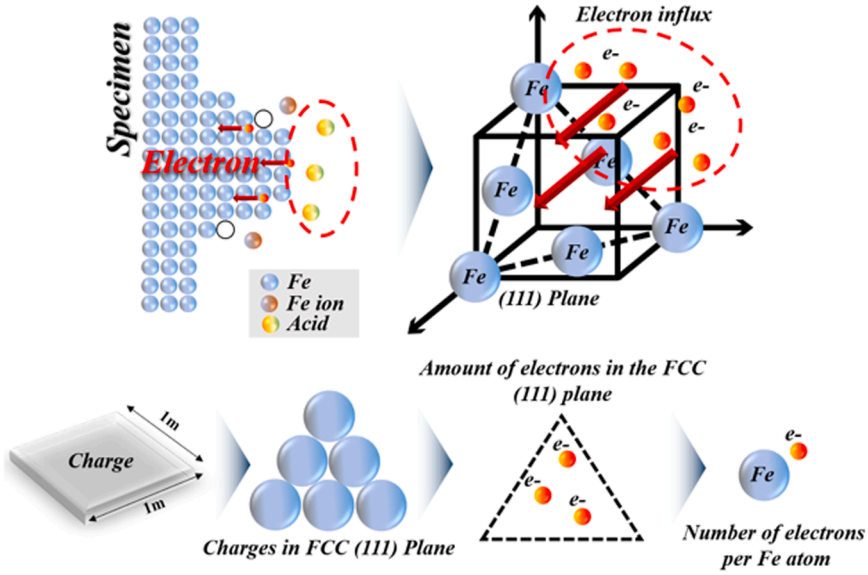

Fig. 10. The conversion process of the areal ion charge density (C/m2) into a number of electrons per single Fe atom for FCC (111) plane; the calculated areal electron charge density can be converted to the number of electrons in the FCC (111) plane by dividing by the following two terms: The area of the FCC (111) plane and the quantity of electron charge. And the number of electrons per single Fe atom is obtained by dividing the number of electrons in the FCC (111) plane by the plane density of the FCC (111) plane.

Table 1
The number of electrons per Fe atom on (111) plane converted from the calculated areal ion charge density.

R_{ku} Electric potential [V]	**2.21** (standard shape)	**1.37**	**1.58**	**3.34**	**4.75**
40	6.00 × 10^{-3}	3.07 × 10^{-3}	3.36 × 10^{-3}	1.03 × 10^{-2}	1.61 × 10^{-2}
30	4.56 × 10^{-3}	2.33 × 10^{-3}	2.92 × 10^{-3}	7.71 × 10^{-3}	1.20 × 10^{-2}
20	3.01 × 10^{-3}	1.55 × 10^{-3}	1.94 × 10^{-3}	5.16 × 10^{-3}	8.00 × 10^{-3}
Base length [nm] Electric potential [V]		**300** (standard shape)	**100**	**500**	**1000**
40		6.00 × 10^{-3}	1.92 × 10^{-2}	3.70 × 10^{-3}	1.92 × 10^{-3}
30		4.56 × 10^{-3}	1.28 × 10^{-2}	2.79 × 10^{-3}	1.28 × 10^{-3}
20		3.01 × 10^{-3}	9.60 × 10^{-3}	1.86 × 10^{-3}	9.60 × 10^{-4}

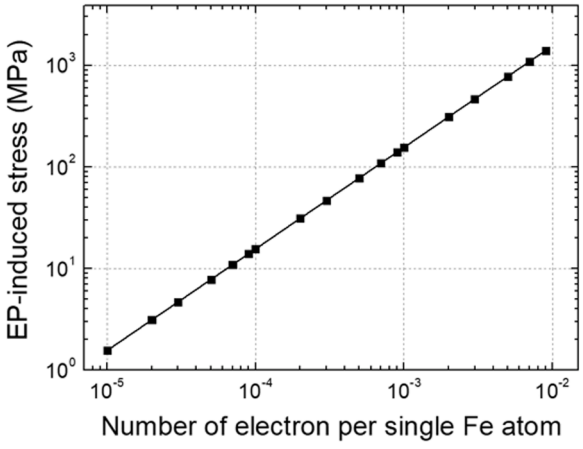

Fig. 11. EP-induced stress caused by the number of electrons per single Fe atom flowing into the asperity.

4.4. Thermodynamic approach for electrochemical polishing induced martensitic transformation

The phase transformation kinetics from metastable austenite to α' martensite is closely related to the free energy of each phase. Fig. 12 shows the free energies of austenite and α' martensite as a function of temperature, which were calculated for a 16Cr-5Ni-0.15C-0.1N-0.9Si-0.3Mn specimen using Thermo-Calc [62].

As shown in this figure, the austenite has metastable characteristics because its free energy is higher than that of α' martensite below the T_0 temperature (560 °C). Thus, below T_0 temperature, the chemical driving force for austenite-to-martensite transformation exists and increases with decreasing temperature. In general, the chemical driving force becomes greater than the activation energy barrier when supercooled below the M_s temperature, resulting in the martensitic transformation. The M_s temperature of the present specimen was calculated to be -87 °C using the following equation [63]:

$$M_s(^{\circ}\mathbf{C}):499 - 308\mathbf{C} - \mathbf{32.4Mn} - \mathbf{27Cr} - \mathbf{16.2Ni} - \mathbf{10.8Si} - \mathbf{10.8Mo} - \mathbf{10.8W}[\mathbf{wt}.\%] \quad (9)$$

As described in Section 4.1, the occurrence of α' martensitic transformation during EP at room temperature, much higher than the M_s temperature, is strong evidence supporting the existence of an additional driving force at room temperature. In Section 4.2, the COMSOL multiphysics simulations and DFT calculations revealed that a significant amount of electric charge gets accumulated in the vicinity of the surface asperities; the charge build-up on the surface asperities results in considerable EP-induced stress as described in Section 4.3. Therefore, the mechanical energy due to the charge build-up may act as an additional driving force for the mechanically induced martensite transformation (MIMT) [64].

The difference between the free energies of the austenite and α' martensite at room temperature was evaluated to be $\Delta G^{\gamma\to\alpha'}_{25^{\circ}C} = 2393$ J/mol (Fig. 12). When the energy difference between $\Delta G^{\gamma\to\alpha'}_{M_s}$ and $\Delta G^{\gamma\to\alpha'}_{25^{\circ}C}$ is added to $\Delta G^{\gamma\to\alpha'}_{25^{\circ}C}$ as a form of mechanical energy, MIMT can occur even at room temperature where EP proceeds. Therefore, U^c indicates a critical mechanical driving force required for MIMT at room temperature and was finally obtained as 303 J/mol. We intended to confirm whether the stress generated by the charge build-up is sufficient enough to cause MIMT by performing the calculation of the interaction energy between EP-induced stress and lattice deformation based on a phenomenological theory [48,65]. Then, the magnitude of the calculated interaction energy was compared with the critical mechanical driving force (U^c) required for the MIMT.

The mechanical interaction energy, U^i, for the i-th variant can be defined by considering the transformation strain for i-th martensitic variant (ε^i_{ij}) and the EP-induced stress (σ^{EP}_{ij}) developed at surface asperities:

$$U^i = m_v \sigma^{EP}_{ij} \cdot \varepsilon^i_{ij} \quad (10)$$

where m_v is the molar volume of the material. To analyze the lattice deformation during the martensitic transformation more precisely, the invariant plane strain (IPS) together with the Bain distortion should be considered based on the crystallographic theory suggested by Wechsler et al. [65]. Here, the K-S orientation relationship with 24 variants was assumed for this lattice deformation. The detailed calculation procedure for the transformation strain for *i-th* martensitic variant (ε^i_{ij}) is described in [48,65]. The variant having the largest energy (U^m) among 24 U^i is energetically favorable, so it is most likely to transform. Eventually, when the U^m value is greater than the critical mechanical driving force (U^c), MIMT due to EP-induced stress can occur.

Referring to the above-described DFT calculation results (Fig. 11), EP-induced stress on the scale of several hundred MPa was generated by the inflow of electrons per Fe atom via (111) plane in the range of 10^{-3} to 10^{-2}. Fig. 13 shows the interaction energy (U^m) at the stress level corresponding to the inflow of electrons per Fe atom in the range of 10^{-3} to 10^{-2} obtained from the DFT calculation.

As shown in the figure, it was confirmed that the interaction energy exceeded the critical mechanical driving force (U^c, 303 J/mol) when the stress of 390 MPa or more was induced. This threshold value of 390 MPa is the stress corresponding to the influx of 2.51 $\times 10^{-3}$ electrons per Fe atom (Fig. 11). Table 1 shows that many more electrons than 2.51 $\times 10^{-3}$ per Fe atom flow into asperities with larger R_{ku} values and shorter base length than into standard asperity (R_{ku} of 2.21 and base length of about 300 nm). In other words, we found that in most asperities the martensitic transformation can occur, since the interaction energy generated by EP-induced stress is greater than the critical mechanical driving force (U^c). In addition to the (111) plane hitherto addressed, we conducted an additional analysis to understand the effect of electrons flowing into the FCC (110) plane of asperity on MIMT and the results presented in Fig. S4 and Table S5 of the supplementary material.

Fig. 14 shows the true stress-strain and work hardening rate curves obtained for the stainless steel through a tensile test. It can be confirmed that α' martensitic transformation starts to occur actively at the inflection point of the work hardening rate curve (a strain of 0.015), and the

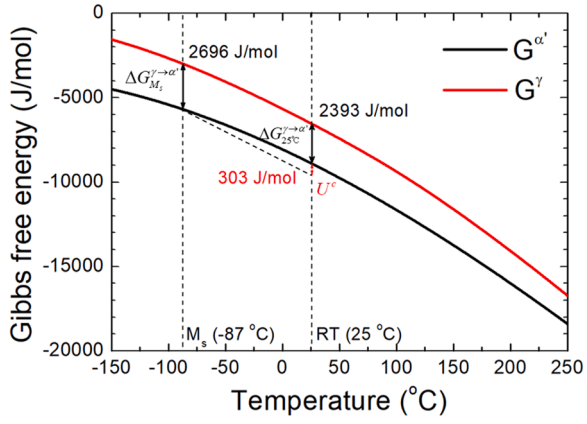

Fig. 12. Temperature-dependent Gibbs free energy change of α' martensite and austenite at room temperature (25 °C) and Ms temperature (-87 °C) calculated by Thermo-Calc.

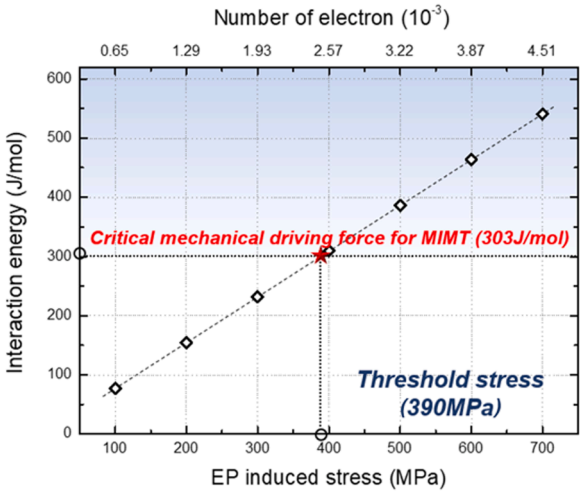

Fig. 13. Interaction energy generated inside the unit cell by EP-induced stress; the number of electrons Fe per atom corresponding to the EP-induced stress are shown in the top axis of the graph from the calculation in Fig. 11.

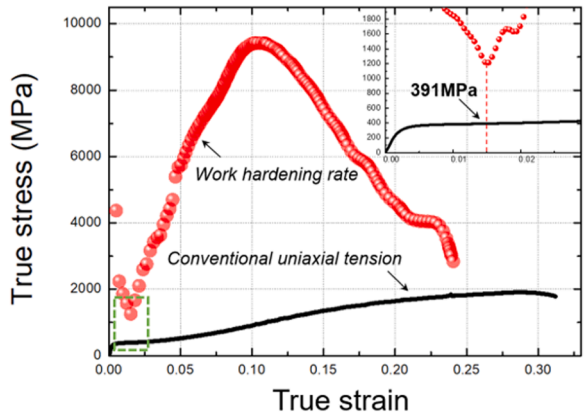

Fig. 14. True stress-strain curve and work hardening rate curve of for 16Cr-5Ni-0.15C-0.1N-0.9Si-0.3Mn (wt.%) stainless steel at room temperature.

stress corresponding to the strain is 391 MPa.

Through this, it was confirmed that the threshold stress, which was obtained using the multiphysics-based finite element simulation, the DFT calculation, and the calculation of the interaction energy, matches well with the experimental martensite formation stress. As a result, we elucidated that the austenite-to-martensitic transformation on the extreme surface of stainless steel during EP treatment is a thermodynamically favorable phenomenon.

5. Conclusion

We discovered an unexpected phenomenon of α' martensitic transformation in 16Cr-5Ni-0.15C-0.1N-0.9Si-0.3Mn (wt.%) stainless steel during EP treatment. By analyzing the EP-treated specimen using EBSD, XRD, and ferritescope, it was found that the formation of α' martensite confined to the extreme surface of stainless steel. To elucidate the mechanism by which α' martensite is generated on the extreme surface during EP treatment, the morphological characteristics of surface asperity were quantified using AFM, and statistical analysis was performed on R_{ku}, R_q, and base length data. Multiphysics-based simulation was performed based on the shape and dimension of asperity to calculate the number of electrons per Fe atom flowing through asperity during EP. The EP-induced stress generated in the unit lattice due to the electron inflow was identified through the DFT calculation. As a result, by analyzing the interaction energy for martensitic transformation under EP-induced stress, it was elucidated that thermodynamically stable α' martensitic transformation in the stainless steel can occur by EP treatment. The main results obtained through this study are as follows.

1 By discovering α' martensite after EP treatment on a fully annealed austenite specimen, we experimentally corroborated that α' martensite phase transformation can occur during EP treatment. Such α' martensitic phase transformation showed a tendency to be promoted as the EP duration and applied voltage increased. And it was found through EBSD, XRD, and ferritescope analysis that α' martensitic transformation was limited to the extreme surface of the specimen. Therefore, these results show that considerable attention is needed when quantitatively analyzing the martensitic transformation of metastable austenite by EBSD or XRD after EP.
2 The areal ion charge density was calculated in various types of asperity through multiphysics-based finite element simulation. Morphological characteristics of asperity were quantitatively identified through atomic force microscopy (AFM) measurement, and various types of asperity were applied to the simulation model based on a statistical analysis of asperity. We could affirm that the smaller the size of the asperity and the sharper it is, the more electric charges are concentrated. At the same time, it was found that the dominant factor affecting the areal ion charge density was the base length of the asperity rather than the R_{ku} value of asperity. When the areal ion charge density calculated through simulation was converted to the number of electrons per Fe atom, 10^{-3} to 10^{-2} electrons flowed into the specimen through asperity.
3 Our DFT calculations showed that excess electrons added to the Fe FCC structure can cause stress linearly depending on themselves. We estimated that 10^{-3} to 10^{-2} excess electrons per Fe atom can flow into asperities during EP, which can induce stress of several hundred or thousand MPa in the system. Such induced applied stress causes self-repulsive interaction leading to possible structural transformation.
4 Thermodynamic analysis was performed to determine whether α' martensitic transformation could occur during EP treatment. Based on the crystallographic theory of Wechsler-Lieberman-Read (W-L-R), we calculated the interaction energy generated during α' martensitic transformation. We also obtained the critical energy for α' martensitic transformation at room temperature through Thermo-Calc. It was found that the EP-induced stress and the interaction energy have a linear proportional relationship, and when the threshold stress of 390 MPa or more was applied, the interaction energy that exceeds the critical martensite transformation energy (303 J/mol) was generated. The experimental tensile test showed that α' martensitic transformation begins to occur actively at a stress of 391 MPa. As a result, it was identified through the interaction energy calculation that EP-induced stress can provide sufficient mechanical driving force for the α' martensitic transformation, which is the evidence for explicating the cause of α' martensite occurrence during EP treatment.

Declaration of Competing Interest

The authors declare that they have no known competing personal relationships or financial interests that could have appeared to affect the work reported in this paper.

Acknowledgments

This work was supported by the National Research Foundation of Korea (NRF) grant funded by the Korean government (MSIT) (Nos. NRF-2020R1A5A6017701, NRF-2021R1A2C3005096, NRF-2019M3D1A1079215, NRF-2018R1A5A1025224, and NRF-2022M3H4A1A02076759). The Institute of Engineering Research at Seoul National University provided research facilities for this work. Some portion of our computational work was done using the resources of the KISTI Supercomputing Center (KSC-2021-CRE-0479 and KSC-2022-CRE-0062).

Supplementary materials

Supplementary material associated with this article can be found, in the online version, at doi:10.1016/j.actamat.2022.118612.

Reference

[1] G. Yang, B. Wang, K. Tawfiq, H. Wei, S. Zhou, G. Chen, Electropolishing of surfaces: theory and applications, Surf. Eng. 33 (2017) 149–166, https://doi.org/10.1080/02670844.2016.1198452.
[2] R.P. Babu, S. Irukuvarghula, A. Harte, M. Preuss, Nature of gallium focused ion beam induced phase transformation in 316L austenitic stainless steel, Acta Mater. 120 (2016) 391–402, https://doi.org/10.1016/j.actamat.2016.08.008.
[3] P. Bała, M. Gajewska, G. Cios, J. Kawałko, M. Wątroba, W. Bednarczyk, R. Dziurka, Effect of Ga+ ion beam on the stability of retained austenite in high carbon steel, Mater. Charact. 186 (2022), 111766, https://doi.org/10.1016/j.matchar.2022.111766.
[4] E.J. Seo, L. Cho, J.K. Kim, J. Mola, L. Zhao, S. Lee, B.C. De Cooman, Focused ion beam-induced displacive phase transformation from austenite to martensite during fabrication of quenched and partitioned steel micro-pillar, J. Alloys Compd. 812 (2020), 152061, https://doi.org/10.1016/j.jallcom.2019.152061.

[5] Q. Yang, L. Qiao, S. Chiovelli, J. Luo, Critical hydrogen charging conditions for martensite transformation and surface cracking in type 304 stainless steel, Scr. Mater. 40 (11) (1999) 1209–1214, https://doi.org/10.1016/S1359-6462(99)00093-7.

[6] R. Fan, J. Magargee, P. Hu, J. Cao, Influence of grain size and grain boundaries on the thermal and mechanical behavior of 70/30 brass under electrically assisted deformation, Mater. Sci. Eng. A 574 (2013) 218–225, https://doi.org/10.1016/j.msea.2013.02.066.

[7] J. Tiwari, P. Pratheesh, O.B. Bembalge, H. Krishnaswamy, M. Amirthalingam, S. K. Panigrahi, Microstructure dependent electroplastic effect in AA 6063 alloy and its nanocomposites, J. Mater. Res. Technol. 12 (2021) 2185–2204, https://doi.org/10.1016/j.jmrt.2021.03.112.

[8] H. Xu, X. Liu, D. Zhang, X. Zhang, Minimizing serrated flow in Al-Mg alloys by electroplasticity, J. Mater. Sci. Technol. 35 (2019) 1108–1112, https://doi.org/10.1016/j.jmst.2018.12.007.

[9] M. Biesuz, T. Saunders, D. Ke, M.J. Reece, C. Hu, S. Grasso, A review of electromagnetic processing of materials (EPM): heating, sintering, joining and forming, J. Mater. Sci. Technol. 69 (2021) 239–272, https://doi.org/10.1016/j.jmst.2020.06.049.

[10] H. Conrad, Electroplasticity in metals and ceramics, Mater. Sci. Eng. A 287 (2000) 276–287, https://doi.org/10.1016/S0921-5093(00)00786-3.

[11] J.T. Roth, I. Loker, D. Mauck, M. Warner, S.F. Golovashchenko, A. Krause, Enhanced formability of 5754 aluminum sheet metal using electric pulsing, Trans. N. Am. Manuf. Res. Inst. SME (2008) 405...412. https://www.scopus.com/inward/record.uri?eid=2-s2.0-52349105676&partnerID=40&md5=e3662227c2d22f0d6d80ad07b881e819https://www.scopus.com/inward/record.uri?eid=2-s2.0-52349105676&partnerID=40&md5=e3662227c2d22f0d6d80ad07b881e819.

[12] A. Lahiri, P. Shanthraj, F. Roters, Understanding the mechanisms of electroplasticity from a crystal plasticity perspective, Model. Simul. Mater. Sci. Eng. 27 (2019), 085006, https://doi.org/10.1088/1361-651X/ab43fc.

[13] M.-J. Kim, S. Yoon, S. Park, H.-J. Jeong, J.-W. Park, K. Kim, J. Jo, T. Heo, S.-T. Hong, S.H. Cho, Y. Kwon, I. Choi, M. Kim, H.N. Han, Elucidating the origin of electroplasticity in metallic materials, Appl. Mater. Today 21 (2020), 100874, https://doi.org/10.1016/j.apmt.2020.100874.

[14] C. Rudolf, R. Goswami, W. Kang, J. Thomas, Effects of electric current on the plastic deformation behavior of pure copper, iron, and titanium, Acta Mater. 209 (2021), 116776, https://doi.org/10.1016/j.actamat.2021.116776.

[15] D. Andre, T. Burlet, F. Körkemeyer, G. Gerstein, J.S.K.-L. Gibson, S. Sandlöbes-Haut, S. Korte-Kerzel, Investigation of the electroplastic effect using nanoindentation, Mater. Des. 183 (2019), 108153, https://doi.org/10.1016/j.matdes.2019.108153.

[16] M.-J. Kim, M.-G. Lee, K. Hariharan, S.-T. Hong, I.-S. Choi, D. Kim, K.H. Oh, H. N. Han, Electric current–assisted deformation behavior of Al-Mg-Si alloy under uniaxial tension, Int. J. Plast. 94 (2017) 148–170, https://doi.org/10.1016/j.ijplas.2016.09.010.

[17] J. Mai, L. Peng, Z. Lin, X. Lai, Experimental study of electrical resistivity and flow stress of stainless steel 316L in electroplastic deformation, Mater. Sci. Eng. A 528 (2011) 3539–3544, https://doi.org/10.1016/j.msea.2011.01.058.

[18] S. Xiang, X. Zhang, Dislocation structure evolution under electroplastic effect, Mater. Sci. Eng. A 761 (2019), 138026, https://doi.org/10.1016/j.msea.2019.138026.

[19] S. Zhao, R. Zhang, Y. Chong, X. Li, A. Abu-Odeh, E. Rothchild, D.C. Chrzan, M. Asta, J.W. Morris, A.M. Minor, Defect reconfiguration in a Ti–Al alloy via electroplasticity, Nat. Mater. 20 (2021) 468–472, https://doi.org/10.1038/s41563-020-00817-z.

[20] A. Ghiotti, S. Bruschi, E. Simonetto, C. Gennari, I. Calliari, P. Bariani, Electroplastic effect on AA1050 aluminium alloy formability, CIRP Ann. 67 (2018) 289–292, https://doi.org/10.1016/j.cirp.2018.04.054.

[21] M.-J. Kim, K. Lee, K.H. Oh, I.-S. Choi, H.-H. Yu, S.-T. Hong, H.N. Han, Electric current-induced annealing during uniaxial tension of aluminum alloy, Scr. Mater. 75 (2014) 58–61, https://doi.org/10.1016/j.scriptamat.2013.11.019.

[22] M. Li, D. Guo, J. Li, S. Zhu, C. Xu, K. Li, Y. Zhao, B. Wei, Q. Zhang, X. Zhang, Achieving heterogeneous structure in hcp Zr via electroplastic rolling, Mater. Sci. Eng. A 722 (2018) 93–98, https://doi.org/10.1016/j.msea.2018.02.106.

[23] P.S. McNeff, B.K. Paul, Electroplasticity effects in Haynes 230, J. Alloys Compd. 829 (2020), 154438, https://doi.org/10.1016/j.jallcom.2020.154438.

[24] W. Wang, R. Li, C. Zou, Z. Chen, W. Wen, T. Wang, G. Yin, Effect of direct current pulses on mechanical and electrical properties of aged Cu–Cr–Zr alloys, Mater. Des. 92 (2016) 135–142, https://doi.org/10.1016/j.matdes.2015.12.013.

[25] J. Zhang, L. Zhan, S. Jia, Effects of electric pulse current on the aging kinetics of 2219 aluminum alloy, Adv. Mater. Sci. Eng. 2014 (2014) 1–8, https://doi.org/10.1155/2014/240879.

[26] H.-J. Jeong, M.-J. Kim, J.-W. Park, C.D. Yim, J.J. Kim, O.D. Kwon, P. P. Madakashira, H.N. Han, Effect of pulsed electric current on dissolution of Mg17Al12 phases in as-extruded AZ91 magnesium alloy, Mater. Sci. Eng. A 684 (2017) 668–676, https://doi.org/10.1016/j.msea.2016.12.103.

[27] Y.S. Zheng, G.Y. Tang, J. Kuang, X.P. Zheng, Effect of electropulse on solid solution treatment of 6061 aluminum alloy, J. Alloys Compd. 615 (2014) 849–853, https://doi.org/10.1016/j.jallcom.2014.07.062.

[28] H.-J. Jeong, M.-J. Kim, S.-J. Choi, J.-W. Park, H. Choi, V.T. Luu, S.-T. Hong, H. N. Han, Microstructure reset-based self-healing method using sub-second electric pulsing for metallic materials, Appl. Mater. Today 20 (2020), 100755, https://doi.org/10.1016/j.apmt.2020.100755.

[29] Z. Tang, H. Du, K. Tao, J. Chen, J. Zhang, Effect of electropulsing on edge stretchability and corrosion resistance near the punched edge of a 2024T4 aluminum alloy sheet, J. Mater. Process. Technol. 263 (2019) 343–355, https://doi.org/10.1016/j.jmatprotec.2018.08.035.

[30] K. Jeong, S.-W. Jin, S.-G. Kang, J.-W. Park, H.-J. Jeong, S.-T. Hong, S.H. Cho, M.-J. Kim, H.N. Han, Athermally enhanced recrystallization kinetics of ultra-low carbon steel via electric current treatment, Acta Mater. 232 (2022), 117925, https://doi.org/10.1016/j.actamat.2022.117925.

[31] COMSOL Multiphysics® version 6.0. www.comsol.com. COMSOL AB, Stockholm, Sweden, Stockholm, Sweden.

[32] A.A. Coelho, TOPAS and TOPAS-Academic: an optimization program integrating computer algebra and crystallographic objects written in C++, J. Appl. Crystallogr. 51 (2018) 210–218, https://doi.org/10.1107/S1600576718000183.

[33] W. Han, F. Fang, Fundamental aspects and recent developments in electropolishing, Int. J. Mach. Tool Manuf. 139 (2019) 1–23, https://doi.org/10.1016/j.ijmachtools.2019.01.001.

[34] M. Petrini, C. Mangano, L. Cellini, M. Di Giulio, G. Iezzi, A. Piattelli, S. D'Ercole, Material characterization and bacterial interaction of titanium discs produced by selective laser melting, Mater. Charact. 189 (2022), 111989, https://doi.org/10.1016/j.matchar.2022.111989.

[35] XEI Data, Processing and Analysis version 1.8.0, Park Systems, Suwon, Korea. https://parksystems.com/manuals-software.

[36] A.Y. Adesina, M. Hussain, A.S. Hakeem, A.S. Mohammed, M.A. Ehsan, A. Sorour, Impact of heating rate on the tribological and corrosion properties of AISI 52100 bearing steel consolidated via spark plasma sintering, Metals Mater. Int. 28 (2022) 2180–2196, https://doi.org/10.1007/s12540-021-01113-4.

[37] E.S. Gadelmawla, M.M. Koura, T.M.A. Maksoud, I.M. Elewa, H.H. Soliman, Roughness parameters, J. Mater. Process. Technol. 123 (2002) 133–145, https://doi.org/10.1016/S0924-0136(02)00060-2.

[38] C. Schotten, T.P. Nicholls, R.A. Bourne, N. Kapur, B.N. Nguyen, C.E. Willans, Making electrochemistry easily accessible to the synthetic chemist, Green Chem. 22 (2020) 3358–3375, https://doi.org/10.1039/D0GC01247E.

[39] E. Łyczkowska-Widłak, P. Lochyński, G. Nawrat, Electrochemical polishing of austenitic stainless steels, Materials (Basel) 13 (2020) 2557, https://doi.org/10.3390/ma13112557.

[40] L.H. Brickwedde, Properties of aqueous solutions of perchloric acid, J. Res. Natl. Bur. Stand. 42 (1949) 309–329, https://doi.org/10.6028/jres.042.026.

[41] A.N. Campbell, J.M.T.M. Gieskes, The dielectric behavior of the system: acetic acid – chloroform – water at 25 °C, Can. J. Chem. 42 (1964) 1379–1387, https://doi.org/10.1139/v64-211.

[42] N.R. Suja, N. Sridevi, K.K. Mohammed Yusuff, A comparative study of catalysis by zeolite encapsulated and neat copper o-phenylenediamine complexes towards oxidation of catechol and 3, 5-di-tert-butylcatechol using hydrogen Peroxide1, Kinet. Catal. 45 (2004) 337–344, https://doi.org/10.1023/B:KICA.0000032166.96733.2c.

[43] AC/DC Module User's Guide, COMSOL Multiphysics® v. 5.6, COMSOL AB, Stockholm, Sweden, (2020), pp. 75–84, https://doc.comsol.com/5.4/doc/com.comsol.help.acdc/ACDCModuleUsersGuide.pdf.

[44] G. Kennell, Free, bound, and mobile charge density, J. Electromagn. Anal. Appl. 9 (2017) 73.

[45] J.W. Jewett, R. Serway, Physics for scientists and engineers with modern physics, Thomson Brooks/Cole, California, 2008.

[46] C. BV, C. OY, COMSOL Multiphysics User's Guide© COPYRIGHT 1998–2010, COMSOL AB, 1998.

[47] G. Kurdjumow, G. Sachs, Über den mechanismus der stahlhärtung, Z. phys. 64 (1930) 325–343.

[48] H.N. Han, C.G. Lee, C.-S. Oh, T.-H. Lee, S.-J. Kim, A model for deformation behavior and mechanically induced martensitic transformation of metastable austenitic steel, Acta Mater. 52 (2004) 5203–5214, https://doi.org/10.1016/j.actamat.2004.07.031.

[49] P. Hohenberg, W. Kohn, Inhomogeneous electron gas, Phys. Rev. 136 (1964) B864–B871, https://doi.org/10.1103/PhysRev.136.B864.

[50] W. Kohn, L.J. Sham, Self-consistent equations including exchange and correlation effects, Phys. Rev. 140 (1965) A1133–A1138, https://doi.org/10.1103/PhysRev.140.A1133.

[51] G. Kresse, J. Hafner, Ab initio molecular dynamics for liquid metals, Phys. Rev. B 47 (1993) 558–561, https://doi.org/10.1103/physrevb.47.558.

[52] G. Kresse, J. Furthmüller, Efficiency of ab-initio total energy calculations for metals and semiconductors using a plane-wave basis set, Comp. Mater. Sci. 6 (1996) 15–50, https://doi.org/10.1016/0927-0256(96)00008-0.

[53] J.P. Perdew, K. Burke, M. Ernzerhof, Generalized gradient approximation made simple, Phys. Rev. Lett. 77 (1996) 3865–3868, https://doi.org/10.1103/PhysRevLett.77.3865.

[54] P.E. Blöchl, Projector augmented-wave method, Phys. Rev. B 50 (1994) 17953–17979, https://doi.org/10.1103/physrevb.50.17953.

[55] H.J. Monkhorst, J.D. Pack, Special points for Brillouin-zone integrations, Phys. Rev. B 13 (1976) 5188–5192, https://doi.org/10.1103/PhysRevB.13.5188.

[56] M. Methfessel, A.T. Paxton, High-precision sampling for Brillouin-zone integration in metals, Phys. Rev. B 40 (1989) 3616–3621, https://doi.org/10.1103/physrevb.40.3616.

[57] V. Kaňa, V. Pernica, A. Zadera, V. Krutiš, Comparison of methods for determining the ferrite content in duplex cast steels, Arch. Foundry Eng. 19 (2019) 85–90, https://doi.org/10.24425/afe.2019.127121.

[58] J. Talonen, P. Aspegren, H. Hänninen, Comparison of different methods for measuring strain induced α-martensite content in austenitic steels, Mater. Sci. Technol. 20 (2004) 1506–1512, https://doi.org/10.1179/026708304X4367.

[59] J.P. Goulmy, P. Kanoute, E. Rouhaud, L. Toualbi, S. Kruch, V. Boyer, J. Badreddine, D. Retraint, A calibration procedure for the assessment of work hardening Part II:

application to shot peened IN718 parts, Mater. Charact. 175 (2021), 111068, https://doi.org/10.1016/j.matchar.2021.111068.
[60] S. Park, J. Jung, K.I. Kim, H. Kim, S.-I. Kim, K.H. Oh, M.-G. Lee, H.N. Han, Practical microstructure-informed dual-scale simulation for predicting hole expansion failure of hyper-burring steel, Int. J. Mech. Sci. 156 (2019) 297–311, https://doi.org/10.1016/j.ijmecsci.2019.04.010.
[61] Y.H. Cho, J. Lee, W.Y. Choo, J. Kang, H.N. Han, Effect of separation on the fracture surface of pipeline steels with ferrite–bainite dual phases during drop weight tear test, Metals Mater. Int. 28 (2022) 1340–1348, https://doi.org/10.1007/s12540-021-00999-4.
[62] J.-O. Andersson, T. Helander, L. Höglund, P. Shi, B. Sundman, Thermo-Calc & DICTRA, computational tools for materials science, CALPHAD 26 (2002) 273–312, https://doi.org/10.1016/S0364-5916(02)00037-8.
[63] P. Payson, Martensite reactions in alloy steels, Trans. Am. Soc. Metals 33 (1944) 261–280.
[64] K.I. Kim, Y. Oh, D.U. Kim, J.-H. Kang, N.I. Cho, K.H. Oh, J.-Y. Kang, H.N. Han, Strain analysis of multi-phase steel using in-situ EBSD tensile testing and digital image correlation, Metals Mater. Int. 28 (2022) 1094–1104, https://doi.org/10.1007/s12540-021-01044-0.
[65] M.S. Wechsler, On the theory of the formation of martensite, Trans. AIME 197 (1953) 1503–1515.